16th International Symposium on Particle Image Velocimetry – ISPIV
2025 June 26–28, 2025, Tokyo, Japan

Volumetric investigation of geometry-induced separation of a turbulent boundary layer

Daniel Schanz[1*], Andrea De Vincenzo[1], Reinhard Geisler[1], Jonathan Lemarechal[1], Tobias Knopp[1], Andreas Schröder[1,2]

1 German Aerospace Center (DLR), Inst. of Aerodynamics and Flow Technology, Göttingen, Germany

2. Institute of Transport Technology, Brandenburg University of Technology, Cottbus, Germany

*daniel.schanz@dlr.de

1. Introduction

Turbulent separated flows are of fundamental importance in a variety of aerodynamic applications, and in particular at the borders of the flight envelope (e.g., at low-speed/high-lift conditions). A main focus of the DLR project ADaMant (Grabe, 2022) is the improvement of the turbulence modeling in Reynolds-Averaged Navier-Stokes (RANS) equations for the correct prediction of the shape and size of turbulent separation bubbles. To enable reliable turbulence model validation and modeling extensions (Eisfeld, 2022), high-quality experimental data are needed. Due to a contradiction in the experimental results of the standard reference test cases for such flows (the Backward-Facing Step Flow (Driver & Seegmiller, 1985) and the NASA Hump Flow (Greenblatt, et al., 2006)), it was decided to design and carry out a new experiment, focusing on geometry-induced separation in a turbulent boundary layer (TBL) at nearly-zero pressure gradient. The experiment was designed to support the further development of the numerical models via data obtained by means of two advanced optical measurement techniques: 2D- and 3D-Lagrangian Particle Tracking (LPT) by Shake-The-Box (STB) (Schröder & Schanz, 2023) (Schanz, et al., 2016) and Temperature-Sensitive Paint (TSP) (Liu, et al., 2005) (Miozzi & Costantini, 2021), which enable the study of the instantaneous and mean flow field features of TBL separation. Here, only the STB results will be presented. A 25° backward-facing ramp, inducing TBL separation, was considered.

2. Experimental setup

For creating a defined separation, a backward-facing ramp model was designed as part of the DLR project ADaMant. To this end, a pretest was performed in the 1-meter-wind-tunnel at DLR Göttingen, where several backward facing ramp geometries were evaluated and the one with the most desired features in terms of reattachment point and recirculation bubble behavior was chosen to be further examined in a larger experiment. This experiment was realized in a water tunnel experiment, where a splitting plate model with included ramp was installed and the resulting flow was examined at four different Reynolds numbers.

To get access to spatially and temporally highly resolved measurements of the TBL flow over the chosen ramp with 25° angle, the advanced 3D LPT method "Shake-The-Box" (STB) has been employed. Both a 2D STB setup in order to characterize the incoming TBL upstream of the step, as well as a two-stage scanning 3D STB setup to fully characterize the flow up- and downstream of the step including the full shear layer development, the recirculation region, the reattachment area and the downstream recovery of the boundary layer flow have been setup. The scanning STB method (Schanz, et al., 2024) allows to increase the achievable volumetric particle density and thus the spatial resolution by alternately illuminating the upper and lower measurement volume and doubling the frequency of the used cameras frame rate. As a result, a high number of Lagrangian Particle tracks including all three components of velocity and acceleration along many time series could be reconstructed. These allow for highly resolved 2D bin averaging results (e.g mean velocity components, 6 x Reynolds stresses and all triple correlations) for the

investigated four various Reynolds numbers, as well as the determination of instantaneous flow structures via data assimilation methods
In the following chapter, the experimental setup used during the STB experiments will be discussed, including the water tunnel, the model, and the equipment employed. Each experimental setup will be discussed in detail in separate sections. Phantom Camera Control (PCC) and LaVision´s DaVis 11 are the software packages used for installing, configuring and controlling the setup, while the complete STB evaluation has been performed with the DLR own STB and FlowFit software packages using CARO HPC resources.

2.1. GWB water tunnel

The water tunnel test was carried out at Großer Wasserkanal Braunschweig (GWB) at the TU Braunschweig, a closed-circuit tunnel characterized by a test section that is 6.0 m long, 1.0 m wide, and 1.0 m high. Experiments can be conducted at different velocities, up to a maximum of 6 m/s. By additionally heating the water, further reducing the kinematic viscosity, Re can be increased without acting on the flow velocity in the channel. The water tunnel can be pressurized up to twice the atmospheric pressure, which allows for a better control of cavitation, one of the major problems in a water tunnel experiment.

2.2. The model

The model used for the GWB water tunnel required specific adaptations, as flow separation was studied using both STB and Temperature Sensitive Paint (TSP) techniques. It was installed vertically in the measuring section, secured to the walls at both the top and bottom. Designed with a 25° backward ramp (step) at 8 mm step height, the model was constructed from anodized aluminum with an interchangeable insert designed for being used with the two techniques. For the STB campaign, the insert consisted of a central glass extending over the step, with horizontal and vertical dimensions of 250 mm and 150 mm, respectively. The use of glass minimizes light reflection at the wall. The model was designed with an elliptic nose to prevent flow separation at the leading edge and a constraint at the trailing edge (TE) to prevent flow separation in that region. The streamwise length was made sufficiently long to allow for flow recovery, while the flat plate was extended to achieve the desired Reynolds numbers Re_X.

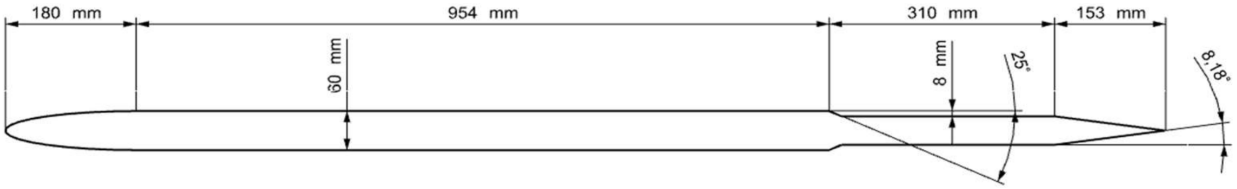

Figure 1: 2D flat plate model with backward-facing step design with 25° ramp for measurements of TBL flows over the step by using STB and TSP at the GWB, TU Braunschweig

2.3. Velocity profile characterization

In a first step of the campaign, a 2D STB measurement was conducted to study the velocity profile of the TBL of the incoming flow in front of the BFS.
A Phantom T4040 camera was coupled to a 200 mm Nikon lens, set to a f-stop of 22 and positioned on the upper side of the tunnel, as shown in Figure 2. For a quick statistical convergence, a chunked recording mode was used. Chunk mode involves breaking down continuous data acquisition into short time sequences (here: 20 consecutive images), termed "chunks". Due to the large separation between successive chunk (50 ms), each chunk is measuring a fresh flow situation, therefore significantly increasing statistical convergence compared to long fully time-resolved sequences. Furthermore, each chunk can by analyzed independently, allowing massive parallelization. As given in Table 1, the acquisition frequency was adapted to the mean flow velocity, ranging up to 9.35 kHz at a camera resolution of 2048 × 1664 pixels. This setup resulted in a total of 2607 chunks per run, each containing 20 images

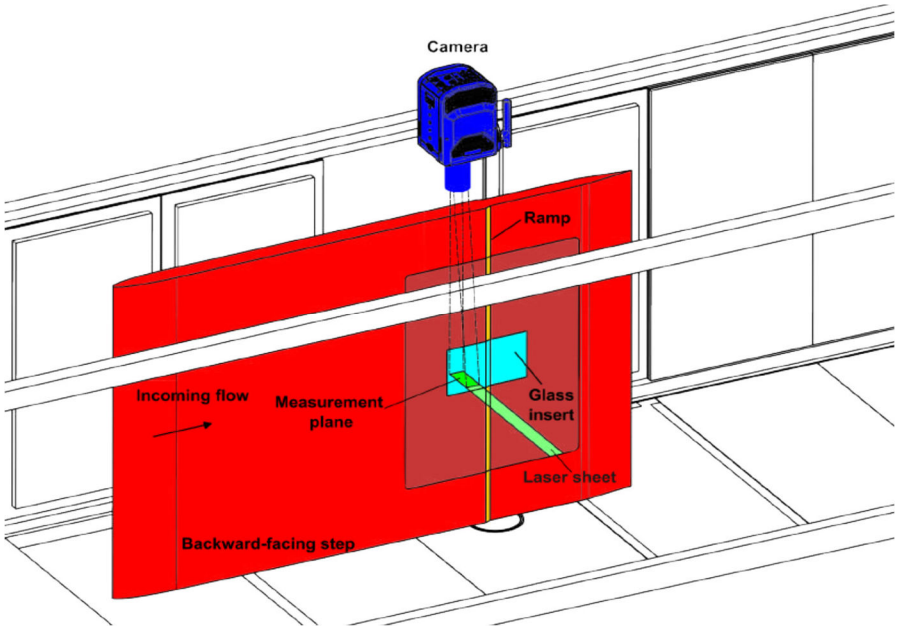

Figure 2: Sketch of the 2D STB set-up for characterization of the incoming TBL profile at GWB

Table 1: TBL velocity profile characterization: water tunnel, camera and laser data corresponding to each tested velocity. The water tunnel was maintained at a constant temperature and pressure throughout all measurements, specifically at T0 = 21.3 °C and P0 = 1 bar.

U $[m/s]$	Re_X	Number of runs	Acquisition frequency $[kHz]$	Number of images	Chunk frequency $[Hz]$	Camera resolution
1.03	1 200 000	6	5.00	20 x 2607	20	2048 x 1664
1.37	1 600 000	6	6.70	20 x 2607	20	2048 x 1664
1.90	2 200 000	7	9.00	20 x 2607	20	2048 x 1664
2.33	2 700 000	6	9.35	20 x 2607	20	2048 x 1664

The light source employed for the profile measurement was a Quantronix Condor E300 (see Figure 4) which is a solid-state laser operated at 1064 nm and converted to 532 nm by using intra-cavity second harmonic generation. The outgoing light beam, is directed through a series of mirrors and lenses, which at the end expanded the beam into a light sheet normal to the flat plate with a streamwise extension of approx. 50 mm and a thickness of approx. 1mm.
To enhance illumination and scattering direction, a back-mirror was installed to equalize the amount of forward and backward scattering for the different cameras. As illustrated in Table 2, the repetition rate increases as the velocity increases. The energy per pulse decrease accordingly. At the same time, the power slightly decreases, likely due to thermal effects.

Table 2: Quantronix Condor E300 performance for the different acquisition frequencies

Repetition rate $[kHz]$	I$[A]$	P$[W]$	E$[mJ]$
5.00	27	39.7	7.9
6.70	27	39.2	5.9
9.00	27	35.6	4.0
9.35	27	35.0	3.7

2.4. 3D STB flow characterization

As the main part of the measurement campaign, a 3D STB experiment was carried out to capture the flow dynamics and flow structures in front of and immediately downstream of the step, capturing the recirculation zone and the separated turbulent shear layer.

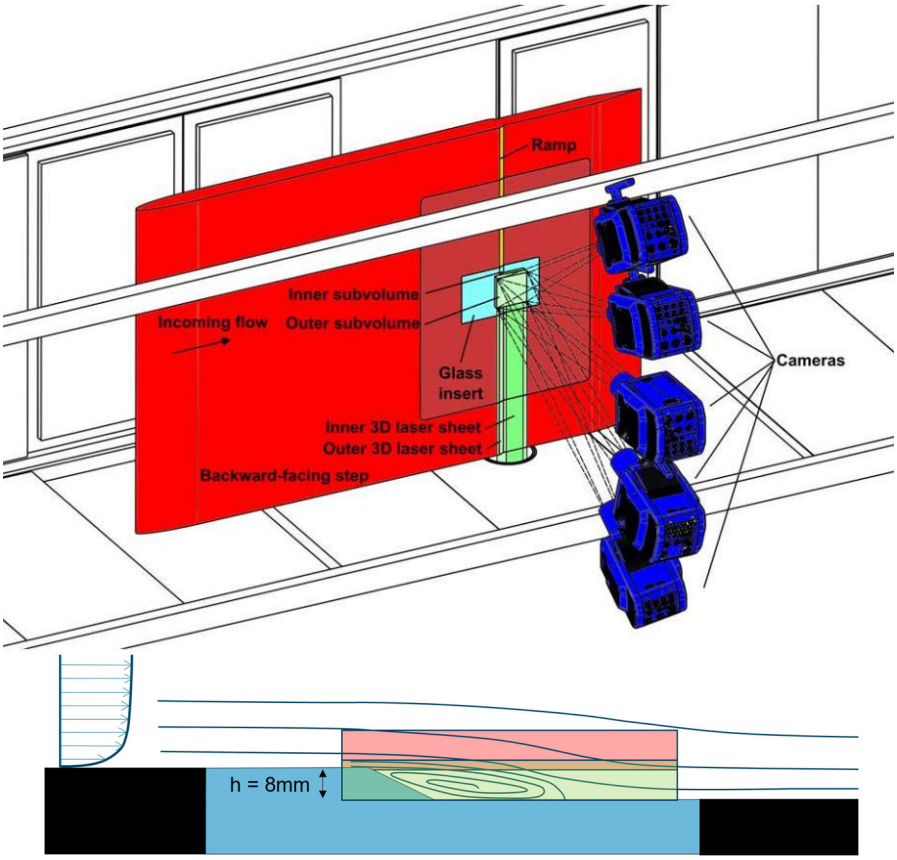

Figure 3: Sketch of the 3D STB setup for measuring the flow over the BFS with ramp (top); illustration of lower (green) and upper (red) sub-volume in relation to the step. Glass insert in blue (bottom).

5 Phantom v2640 cameras were employed, each featuring 4- megapixel (Mpx) 12-bit CMOS image sensors, capable of recording at 6600 fps at full resolution. The cameras were paired with Carl Zeiss 100 mm Makro-Planar lenses and positioned as illustrated in Figure 3. Teleconverters were used with the two outer cameras with longest viewing distances. Scheimpflug adapters were used to keep all particles in focus. The total volume of interest was divided into two wall-parallel sub-volumes, which were illuminated intermittently by two different laser heads (see Figure 3 (bottom)). Each subvolume had a depth of approximately 8 mm.

The cameras were operated at double the laser frequency, thereby capturing the lower volume in every even frame and the upper volume in every odd frame. This approach allows increasing the particle concentration within the measurement volume (particles-per-volume, ppv), while limiting the imaged particle density (particles-per-pixel, ppp).

Three fully time-resolved runs, filling the full camera memory of 144GB, were performed for each of the four considered Reynolds numbers. Due to the huge temporal scale separation that characterizes the separated turbulent flow field, a chunk image acquisition was used as well in order to acquire a large number of statistically independent flow states (see Table 3). A total of 2.800 to 5.250 chunks, each consisting of 30 consecutive time-steps, was recorded for each Reynolds number.

Table 3: Experimental details of the chunk-based 3D-STB measurements.

U $[m/s]$	Re_X	T_0 $[°C]$	Number of runs	Acquisition frequency $[kHz]$	Number of images	Chunk frequency $[Hz]$	Δt $[\mu s]$	Camera resolution
1.03	1 200 000	21.3	28	3.00 x 2	30 x 100 x 2	2	166.567	2048 x 1952
1.37	1 600 000	21.4	30	4.50 x 2	30 x 100 x 2	2	111.000	2048 x 1416
1.89	2 200 000	21.5	27	6.00 x 2	30 x 150 x 2	3	83.000	2048 x 1056
2.31	2 700 000	21.6	30	7.50 x 2	30 x 175 x 2	4	66.567	2048 x 832

The camera resolution had to be adjusted to account for the increasing acquisition frequency, while also considering the presence of the two sub-volumes. For the 3D STB measurement, two Photonics Industries DM200 series Dual Head Nd:YAG green nanosecond lasers were employed (see Figure 4).

Figure 4: 2 Photonics DM200 series Nd:YAG lasers for the 3D STB measurement volume illumination (mid) and a Quantronix Condor E300 for the 2D STB TBL profile measurement (left)

The laser beams were spatially separated and guided through suitable lenses and mirrors to generate a 3D light volume, separated into two subvolumes, each measuring 8 mm in width and 90 mm in height. The two beams were temporally separated by setting a time delay $\Delta t = 1/(2*f)$. Table 4 illustrates how the supplied current, power output and energy per pulse behaved at different repetition frequencies.

Table 4 Photonics DM200 series performance for the different acquisition frequencies

Repetition rate $[kHz]$	Photonics DM200 L1			Photonics DM200 L2		
	I [A]	P [W]	E [mJ]	I [A]	P [W]	E [mJ]
3.0	29.5	72	24.0	27.5	70	23.3
4.0	29.5	85	18.9	27.5	82	18.2
6.0	32.5	117	19.5	30.5	120	20.0
7.5	32.5	122	16.3	30.5	128	17.1

2.5. Seeding

The choice of the seeding material is fundamental in order to achieve high-quality LPT results and to accurately capture flow structures, as well as ensuring homogeneous distribution of particles in the fluid. For this flow study, ORGASOL® 2002 D NAT 1 particles were used (https://hpp.arkema.com/en/products/product/f/spa_hpp_Orgasol/p/orgasol-2002-d-nat-1/). They are spheroidal polyamide with a narrow particle size distribution and an average diameter of 20 µm, with a density of $\rho = 1.02$ g/cm^3. To evaluate the effectiveness of these particles in representing the fluid flow, the Stokes number (Sk) is now estimated. This dimensionless parameter is representative of how well the particles follow rapid changes in the flow. In particular, the condition $Sk << 0.1$ returns an acceptable flow tracing. For the current investigation, Stokes numbers well below 0.01 are estimated for all Reynolds numbers. Unfortunately, the particles were found to scatter light with a relatively strong dependence on their rotation direction.

3. Characterization of the incoming TBL flow

Using 2D STB (Schröder, et al., 2018) a characterization of the u- and v-components of individual particle tracks within the turbulent boundary flow between x = -111 mm and -66 mm upstream of the step has been performed. Each of the over 15,000 chunks recorded per Reynolds number, consisting of 20 consecutive images each, was processed by a two-pass 2D-STB process. After the second pass, typically around 15,000 particles are tracked per time-step.

Figure 5 (left) shows an exemplary stack of three consecutive snapshots of the camera image, while Figure 5 (middle) shows an instantaneous evaluation result by plotting velocity vectors, color-coded by streamwise velocity. For statistic evaluation, the tracks are treated by a bin-average process. Figure 5 (right) displays the result of a 2D grid of bins of size 5,000 µm x 10 µm. In all images, the wall is visible as a line with close to zero velocity. The reflections of particle images at the wall can be recognized in the lowest part of the image and lead to a mirrored profile.

Very close to the wall for y < 80 µm the strong shear flow leads to a rotation of the 20 µm polyamide particles and thus to strong variations of the image intensity along the time-series and furthermore the scattered light of the particle and the mirrored particle image on the glass surface added to uncertainties due to interference effects of the coherent laser light.

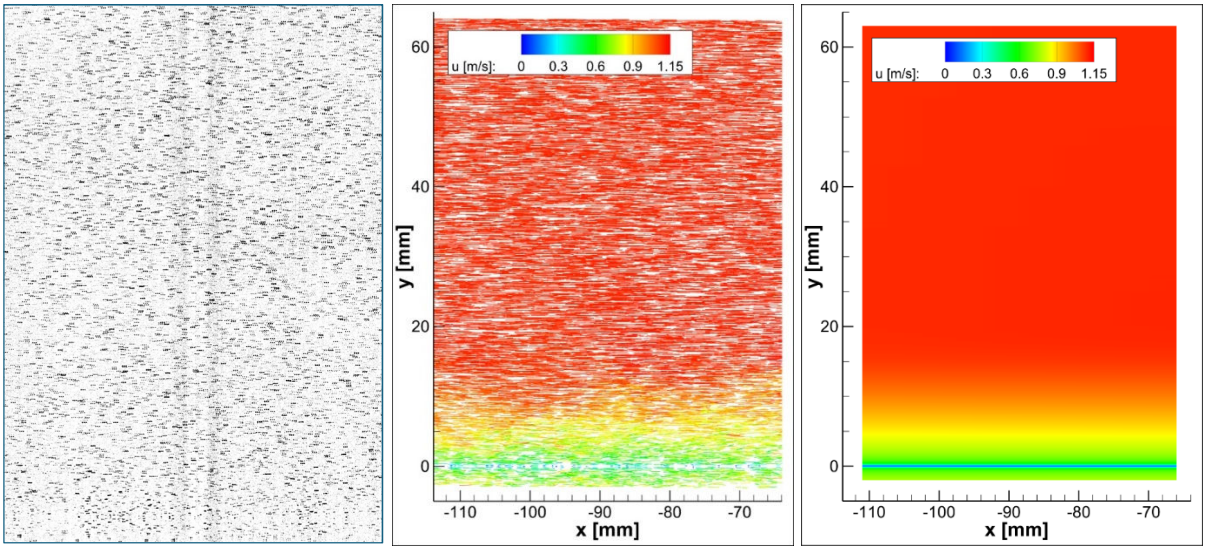

Figure 5: Sum of three consecutive camera images of the 2D inflow measurement after subtraction of a minimum image (left); instantaneous particle tracks (left) and corresponding bin averaging result in a grid of 5,000 x 10 µm² bins (right) for Re = 1,2 x 10^6. (x, y) = (0, 0) mm at the front step.

Both effects lead to shorter tracks and some ghost tracks, which need further investigations and more adapted image processing schemes e.g. tracking with visible time steps of a particle image only and solving the parallaxes problem of the particle position with respect to the wall. Furthermore, ideas of using the new developed Peak-CNN detector (Godbersen, et al., 2024) to resolve overlapping of direct- and mirror-counterpart particle images directly at the surface are under discussion.

Profiles of velocity and Reynolds stresses are created by binning along the whole streamwise extent of the measurement area with 10 µm bin sizes in wall normal- or y- direction for all four Reynolds numbers (see Figure 6 and Figure 7). The very-near-wall region had to be cut away due to the problems mentioned above.

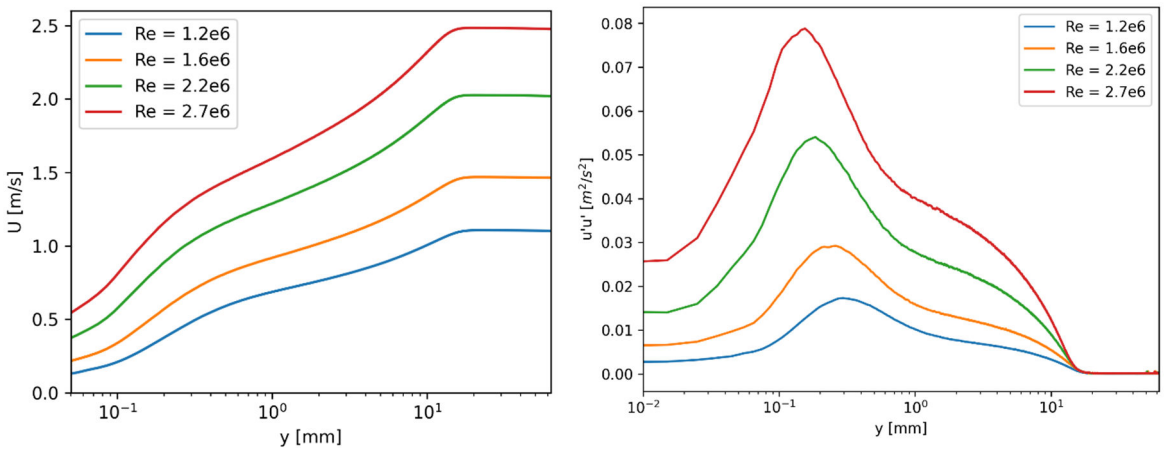

Figure 6: Mean velocity profiles in half-logarithmic scaling of physical quantities (not normalized) for all four measured Reynolds numbers (left) and corresponding u'u'-profiles (right).

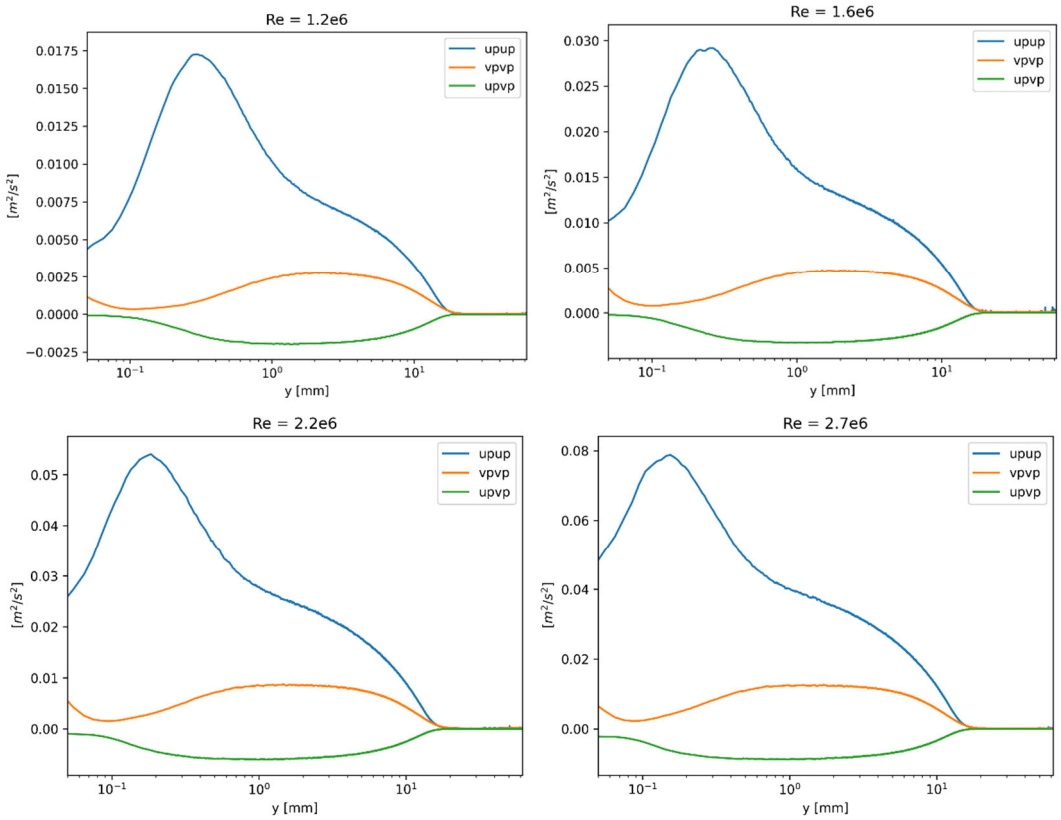

Figure 7: Reynolds stress components for the four Reynolds numbers plotted in a half-logarithmic scale presenting physical quantities (not normalized).

4. 3D-characterization of the ramp region

Evaluation of the 3D experiments consisted of application of Variable-Timestep STB (Schanz, et al., 2021) for both sub-volumes and subsequent FlowFit3 data assimilation (Godbersen, et al., 2024). For the lower volume, where strong differences in the average velocities are encountered due to the presence of the recirculation bubble, four VT-STB passes with the following properties are performed for the fully time-resolved runs: (10_f, 2_b, 1_f, 1_b), where the number signifies the fraction of used timesteps (dt) and the subscript denotes the direction of time (f: forwards in time; b: forwards in time). The long time separation of the first pass (dt = 10) allows to accurately track the slowly moving particles close to the walls, as well as the not-moving particles sticking to them (in total typically around 2,000- 3,000).

The second pass, increasing the temporal resolution to dt = 2 allows to track the particles with low accelerations in all velocity regimes (around 70,000), while the two passes at dt = 1 will add the particles in accelerated regions and help to fill up and reconnect partial tracks from the preceding passes. In total around 120,000 particles are typically tracked in the lower volume after pass 4. For the evaluation of chunked runs, the first pass was reduced to dt = 5, as the time-series length of 30 consecutive images would otherwise limit the track length too much.

For the upper volume, only two passes at the full sampling frequency (1_f, 1_b) are performed, as this volume is mostly dominated by the highly active shear layer above the recirculation bubble and by the fast bulk flow. Typically, around 145,000 particles are tracked within the upper volume in the first pass and around 160,000 in the second. Accounting for the overlap region of approx. 3 mm, around 250,000 are typically tracked within the full volume in every time-step. These values were determined for the Re_X = 1.2e6 – case, where the cameras could use the full sensor. For the higher Reynolds-number cases, the number of tracked particles reduces with the camera resolution (which limits the spanwise width of the reconstructed volume).

Vibrations of the water tunnel structure are determined by averaging the positional shift of the know particle sticking to the model (typically a few hundred). The high positional accuracy combined with the relevant number of particles allows to correct for wall vibrations in the order of 1 µm. Figure 8 illustrates that for the wall-normal vibration we recognize an amplitude of approx. ± 4 µm.

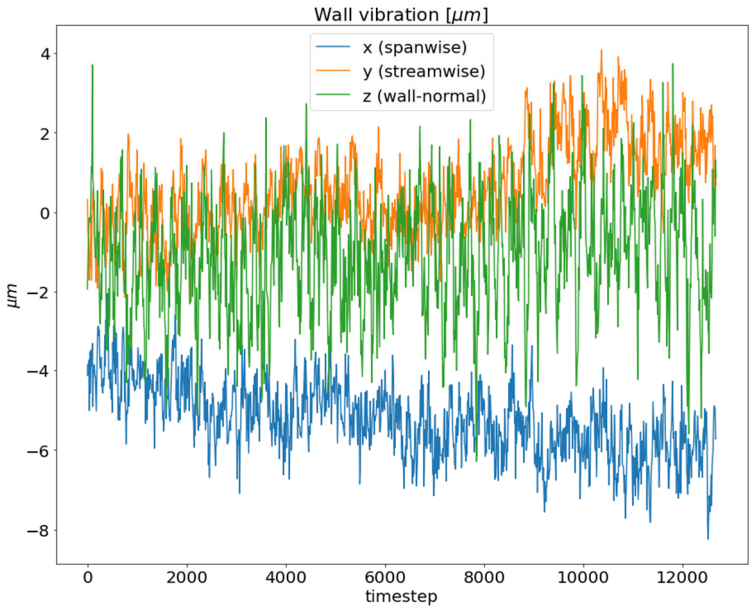

Figure 8: Wall vibrations in all three dimensions of space, determined by tracking the particles sticking to the model wall and averaging their displacement from a ground state

Figure 9 shows exemplary visualizations of a tracked particle field. Plotted are velocity vectors of ten subsequent time-steps, color-coded by u-velocity in the full volume and in two thin wall-parallel slices, representing the streaky nature of the boundary and free-shear layer flow (middle) and the near wall flow organization (bottom), which will be directly compared to TSP results (not shown here).

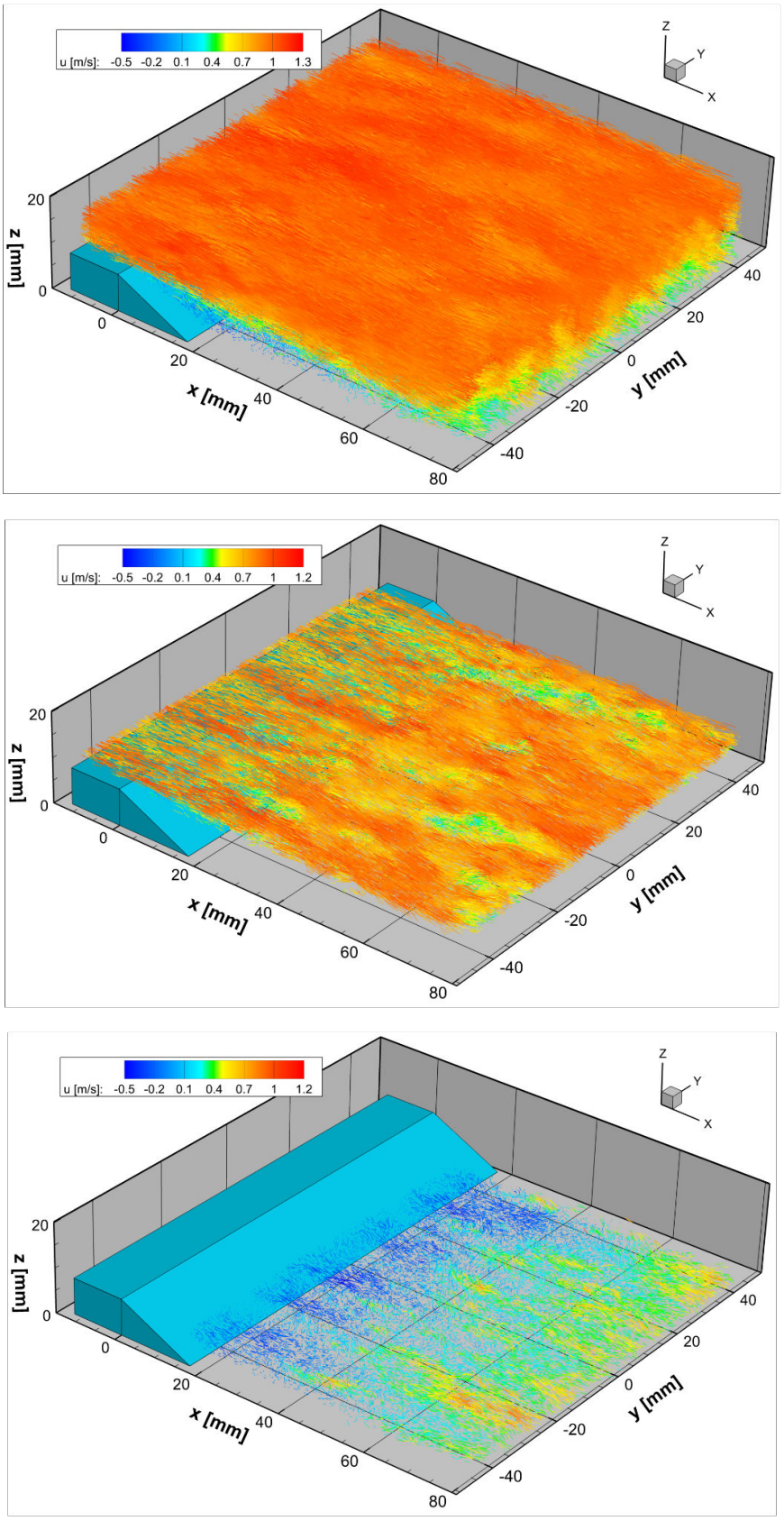

Figure 9: Subsample of 10 time-steps of reconstructed tracks within the whole measurement volume (top), a slice in the lower separated TBL flow (middle) and the downstream near-wall region (bottom).

By performing regularized spatial interpolation onto a regular grid using the data assimilation method FlowFit3, it is possible to visualize the temporal and spatial evolution of coherent flow structures. FlowFit3 was applied to individual time-steps of the time-resolved STB runs, resulting in a continuous flow field representation in a staggered grid of 3D cells with spacing h = 0.5 mm using mixed 3rd- and 4th-order B-splines, allowing e.g. to visualize vortex structures via the Q-criterion Q = 7 × 10^3 1/s^2. At the edge, the boundary layer separates and a shear layer starts to form, which is mainly dominated by Kelvin-Helmholtz instabilities embedded into the highly turbulent shear flow motion. These arise due to the velocity gradient between the separated shear layer and the surrounding flow, and roll up into spanwise vortices that remain large scale and spanwise aligned (approximately $0 \leq x \leq 20$ in Figure 9-23), interacting primarily with the freestream flow. Further downstream, the shear layer develops, growing thicker and bending downward, characterized by high and low speed streaks.
Beneath the shear layer, a large recirculation region forms. Within this area, counter-rotating vortices develop as the high-speed shear layer interacts with the low-momentum recirculating fluid, resulting in structures that continuously stretch, tilt, and break down into smaller scale eddies. Figure 9-23 shows this process through dense clusters of small-scale vortices. The evolution of these vortical structures influences the overall flow dynamics, especially the length of the separation bubble, the location of reattachment, and the intensity of the Reynolds stresses.

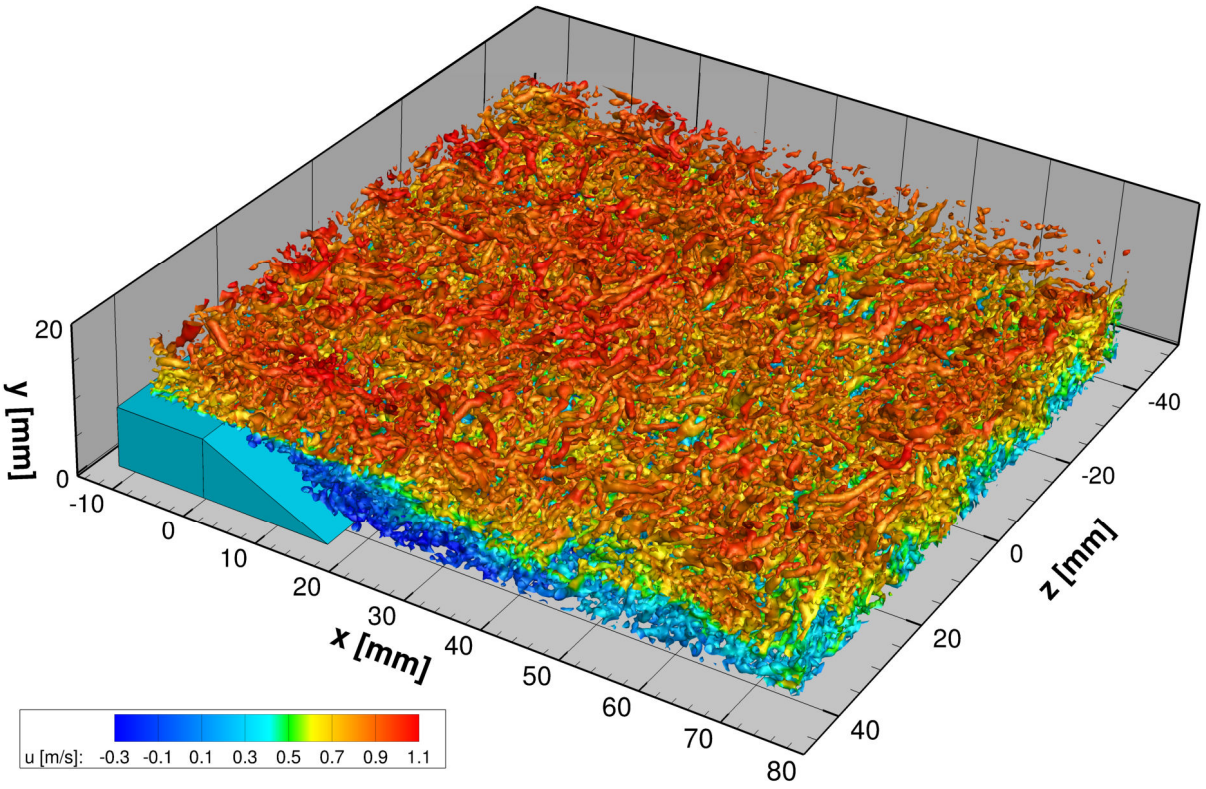

Figure 10: Snapshot of FlowFit3 reconstructions at Re = 1.2 x 10^6. Vortical structures revealed by iso-surfaces of Q-criterion at 7 × 10^3 [1/s^2], color coded by u -velocity.

4.1.Statistics of the ramp region

Statistics were again evaluated using a bin-averaging approach, here applied within 3D bins of bins of $\Delta x = 400 \times \Delta y = 20$ µm and using the whole spanwise domain. Figure 11 illustrates the average light intensity, as well as number of particles present in each bin. It is clearly visible that the laser used for the upper volume has a higher output compared to the lower one and has a Gaussian intensity profile. Reflections on the inclined step increase the illumination of regions close to it. Several effects of inhomogenous illumination are visible. The upper laser shows diffraction effects at the front and back end of the volume and a pattern is visible in the center of the volume (x = 50 mm), which might be attributed to an imperfection on one of the lenses or mirrors. The lower laser shows a large circular interference pattern and, most notably a stripy diffraction pattern close to the wall (see detail view). Most of these defects leave minor traces in the tracking. The number of tracked particles scales with the mean intensity, as smaller particles might become visible or invisible. This effect is most prominent in the near-wall region, where the number of found particles follows the same stripy pattern as the average illumination.

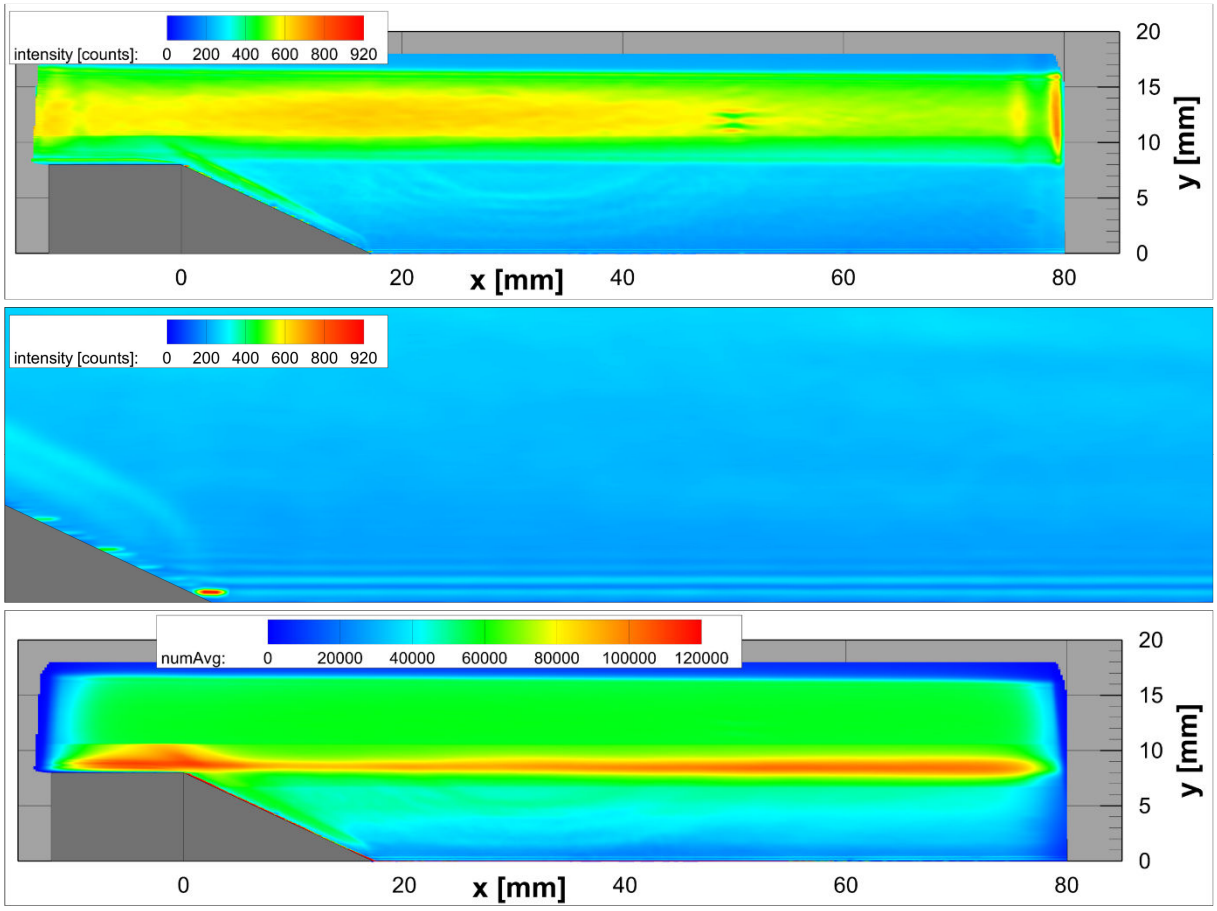

Figure 11: Average intensity (top) and a detail view of the same at the foot of the step (middle); number of entries per 200 µm × 20 µm bin for the full domain (bottom). Bins extend over the full span.

Due to the large number of time-steps and particles, each bin is populated by at least 20.000 particles, despite its small size. Less particles are found in the lower volume due to the intensity difference. The overlap region is readily visible as a line of high particle number per bin, as here particles may be counted double. Very close to the wall, high values are attained due to the sticking particles that are present within every time-step. The grid discussed here (‘Grid 1’) is well applicable to near-wall

problems due to its high wall-normal resolution. For other studies a rectangular grid ($\Delta x = 126.5 \times \Delta y = 126.5$ µm, 'Grid 2') is applied.

4.1.1. Velocity statistics

Figure 12 illustrates the mean flow structure and velocity fields in the backward-facing ramp geometry, averaged on Grid 2. The ramp is shown in gray on the left, while the main flow proceeds from left to right. The fluid enters from the top-left with relatively high momentum, and then passes over the step edge. At this point, the flow separates, giving rise to a shear layer that reattaches farther downstream. As depicted in Figure 12 (top), the streamwise velocity remains relatively high in the region above the ramp, since the free-stream fluid is largely unimpeded in that zone. In contrast, a recirculation zone is present immediately after the step. Within this bubble, a portion of the fluid near the wall flows upstream relative to the main flow. This upstream motion is sustained by entrainment and momentum transfer from the faster shear layer located above. Because the shear layer is unbounded below, it falls under the class of free shear flows and thus, it is prone to Kelvin–Helmholtz instabilities. This is typically associated with strong shear in laminar or weakly turbulent flows. In a fully developed turbulent shear layer, multiple scales of motion coexist, including streaks and other coherent structures, making a direct interpretation in terms of classical Kelvin–Helmholtz instability less straightforward. However, by applying 3D two-point correlation, it is generally possible to analyze the coherent component of turbulence, performing a form of spectral decomposition. This should identify instability waves within the shear layer, even though their presence may not be clear in instantaneous velocity snapshots. Although Figure 12 does not capture instantaneous vortical structures, it is possible to deduce their presence from the strong velocity gradients. These coherent structures, formed via vortex roll-up, usually merge into larger eddies through vortex pairing, as the flow progresses downstream. Once it convects downstream, the shear layer ultimately reattaches to the bottom surface. It is important to note that the reattachment point is not fixed in space, instead it is subjected to low-frequency "flapping" of the separated shear layer, which can oscillate vertically and horizontally. This unsteadiness is strictly connected to the formation and shedding of large-scale vortices that lie within the wake of the ramp. As these vortices convect downstream, they intermittently alter the local pressure field and momentum flux, causing the reattachment location to oscillate.

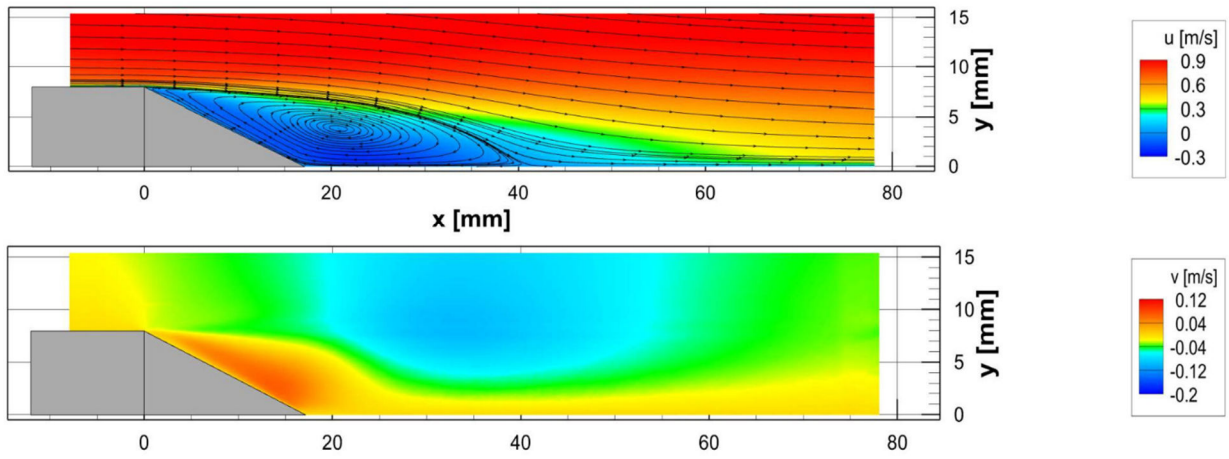

Figure 12: Time- and spanwise-averaged velocity distributions of u (top) and v (bottom) at Re = 1.2 x 10^6. Results from averaging 3D STB results in bins of 200 µm streamwise, 20 µm wall-normal.

The v component (see Figure 12 (bottom)) is nearly one order of magnitude smaller than the streamwise component. This is related to the mixing processes in the flow. Indeed, region characterized by positive mean values represent fluid moving upwards, mainly because of the shear layer pulling fluid from the recirculation zone into the higher-speed outer flow. Instead, negative values of the wall normal velocity component indicate a downward movement of the flow, either by the large-scale eddies that form within the shear layer or by local pressure gradients.

4.1.2. Determination of the reattachment length

Determining the reattachment length requires to identify the streamwise point, where the average streamwise velocity changes from negative to positive. Due to the mentioned illumination issues very close to the wall and the presence of sticky particles this property shows some uncertainties. However, an attempt to determine the mean reattachment length is now presented.

The reattachment zone is characterized by a backward flow upstream of the reattachment point, which induces negative wall shear stress. However, as soon as the flow transitions to forward motion, downstream of this point, the wall shear stress turns positive. This transition is directly linked to the gradient of u in y-direction near the wall, as the shear stress at the wall is proportional to this quantity:

$$\tau_w = \mu \frac{\partial u}{\partial y}\bigg|_{y=0}$$

where τ_w is the wall shear stress, μ is the dynamic viscosity of the fluid, and $\partial u/\partial y$ is the velocity gradient. The zero crossing of the wall shear stress defines the reattachment point, as it reflects the change in sign of τ_w.

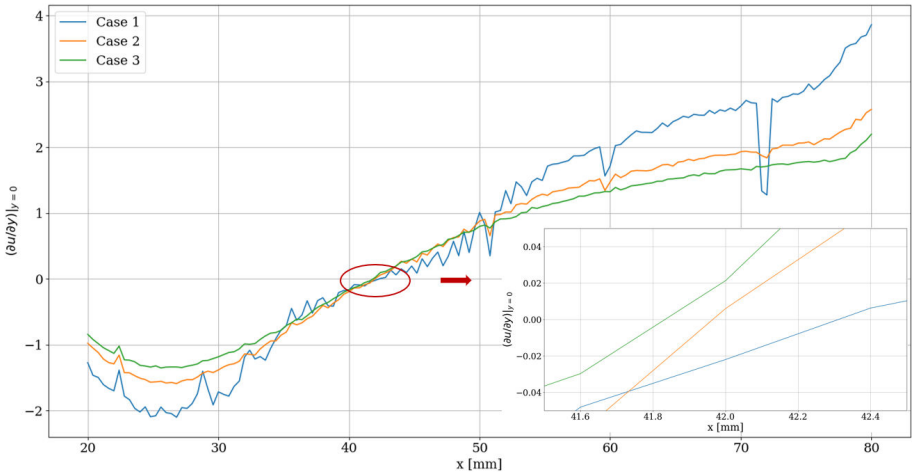

Figure 13: Reattachment length evaluation, considering three different cases. Case 1, Case 2 and Case 3 consider a wall normal distance to evaluate the u2 respectively of 0.02, 0.04 and 0.06 mm.

To evaluate the gradient of the streamwise velocity component at the wall, a finite difference approach was employed, considering three different positions close to the surface:

$$\frac{\partial u}{\partial y}\bigg|_{y=0} \approx \frac{u_2 - u_1}{y_2 - y_1}$$

with $u_1 = 0$ m/s representing the velocity at the wall, and $y_1 = 0$ mm being the wall distance. Instead, y_2 corresponds to the different position for the 3 cases, with u_2 denoting the respective mean velocities along the wall parallel bins across the streamwise direction. Figure 13 provides an estimation for the different cases, highlighting also the illumination problem, and how the situation improves with increasing the distance is considered. However, a less precise evaluation of $\partial u/\partial y$ is obtained for larger values of y_2. To our opinion, the reattachment length can be approximated by considering Case 2, which estimates it at x = 41.9 mm.

4.1.3. Reynolds stresses

The 3D nature of the data allows to evaluate all 6 components of Reynolds stresses, which are defined as the covariance of the velocity fluctuations and allow to define the Reynolds stresses tensor, which is written as:

$$\tau_{ij} = \begin{bmatrix} \overline{u'u'} & \overline{u'v'} & \overline{u'w'} \\ \overline{v'u'} & \overline{v'v'} & \overline{v'w'} \\ \overline{w'u'} & \overline{w'v'} & \overline{w'w'} \end{bmatrix}$$

with the diagonal terms referring to the normal stresses, and the extra-diagonal to the shear stresses. They represent how turbulence transports momentum within the flow. The grid employed for this evaluation was again Grid 2, which should be able to capture in a more precise manner the interactions in different directions between velocity fluctuations.

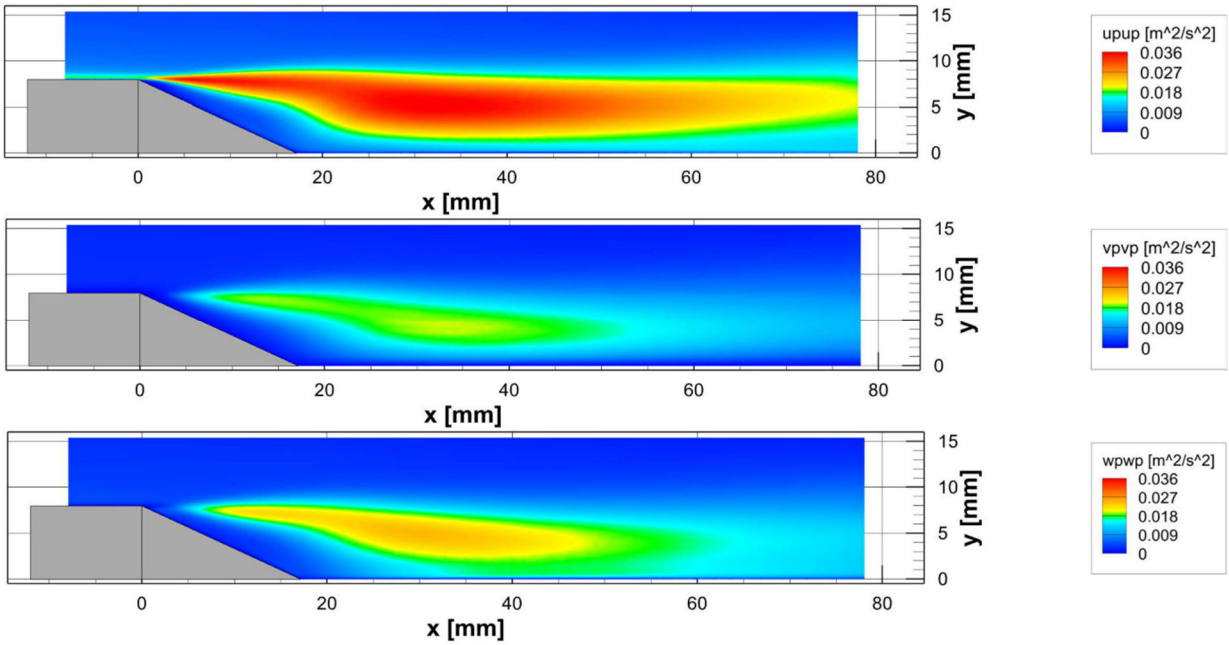

Figure 14: Time- and spanwise-averaged Reynolds stresses distributions of u'u', v'v' and w'w'

The three Reynolds stresses components show a distribution which extends in the free shear layer (from x ≈ 0 mm to x ≈ 40 mm) due to the high level of mixing rate, and therefore a high level of turbulence. They start from the separation point of the ramp, and quickly increase in both intensity and width, along

the streamwise direction. A peak can be identified at approximately x = 30 mm. At approximately x = 20 mm, the distributions in Figure 9-14 experience a change in shape, with a kink appearing.
In order to understand the flow behavior in this region, it may be helpful to refer to the streamline superimposition of the streamwise acceleration ax (see Figure 16). It is clear that the change in the Reynolds stresses behavior coincides with the pressure jump, with particles exhibiting strong acceleration (blue region of negative velocity in the lower-right part of the recirculation bubble). The recirculating flow is subjected to compression, followed by relaxation closer to the ramp, accompanied by a strong pressure gradient within the flow. Due to the squeezing effect near the wall, the flow accelerates and consequently, turbulence amplitudes are dampened. As soon as the flow opens again, a deceleration of the local flow leads to a large increase in turbulence production, altering the Reynolds stresses distributions, resulting in the observed shape change.

4.1.4. Triple-correlations

The wealth of available data allows to evaluate statistically converged 2D fields of triple correlations. Figure 15 shows two selected entries (u'u'v' and v'v'u'). It can be seen that the regions of high activity in the triple correlations extend quite far downstream, likely being dominated by the strong u' component. For the whole region behind the step, they exhibit a zero-crossing, whose positions roughly coincides with the location of the maximum Reynolds stresses.

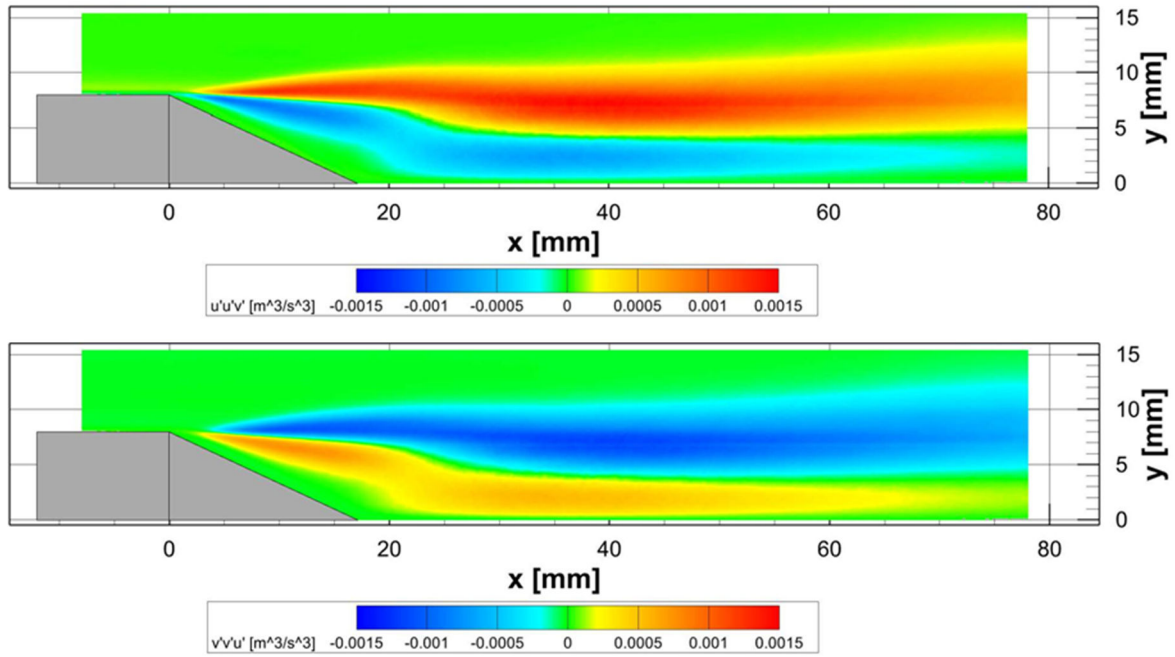

Figure 15: Time- and spanwise-averaged triple-correlations u'u'v' and v'v'u'

4.1.5. Accelerations

Time- and spanwise- averaged streamwise and vertical accelerations distribution are shown in Figure 16. By observing Navier-Stokes momentum equation below, it is clear that a measure of the accelerations provides valuable information about how pressure gradients act on the flow.

$$\frac{D\mathbf{u}}{Dt} = \frac{\partial u}{\partial t} + u \cdot \nabla u = \mathbf{a} = -\frac{1}{\rho}\nabla p + \mathbf{g} + \nu\nabla^2\mathbf{u}$$

With an initial a_x component due to the presence of the model itself, the flow experiences an increase in the streamwise acceleration on top of the edge due to the presence of a suction peak. This identifies the presence of a pressure minimum (strong red peak slightly before the ramp), which eventually turns into a deceleration as soon as separation occurs (blue region in Figure 16 (top)). Downstream of the edge, the shear layer is starting to developing and widening vertically, a pressure reduction occurs and the flow starts to accelerate again due to a "squeezing effect". This is caused by the reduction in flow area, as the shear layer interacts with the wall below. As soon as the pressure gradient relaxes instead, the flow decelerates very quickly, producing the jump clearly shown in Figure 16. After reattachment, the flow normalizes to a zero-pressure gradient further downstream, resulting in an almost negligible acceleration in the streamwise direction. In the shear layer region, large scale vortices form and convect downstream. This implies that positive or negative peaks reflect the center, in the mean sense, of these turbulent structures. The upward movement of the flow, as influenced by the shear layer, causes it to bend slightly, introducing asymmetry in the layer's vertical development, which is a result of the upward flow motion originating from the recirculation region.

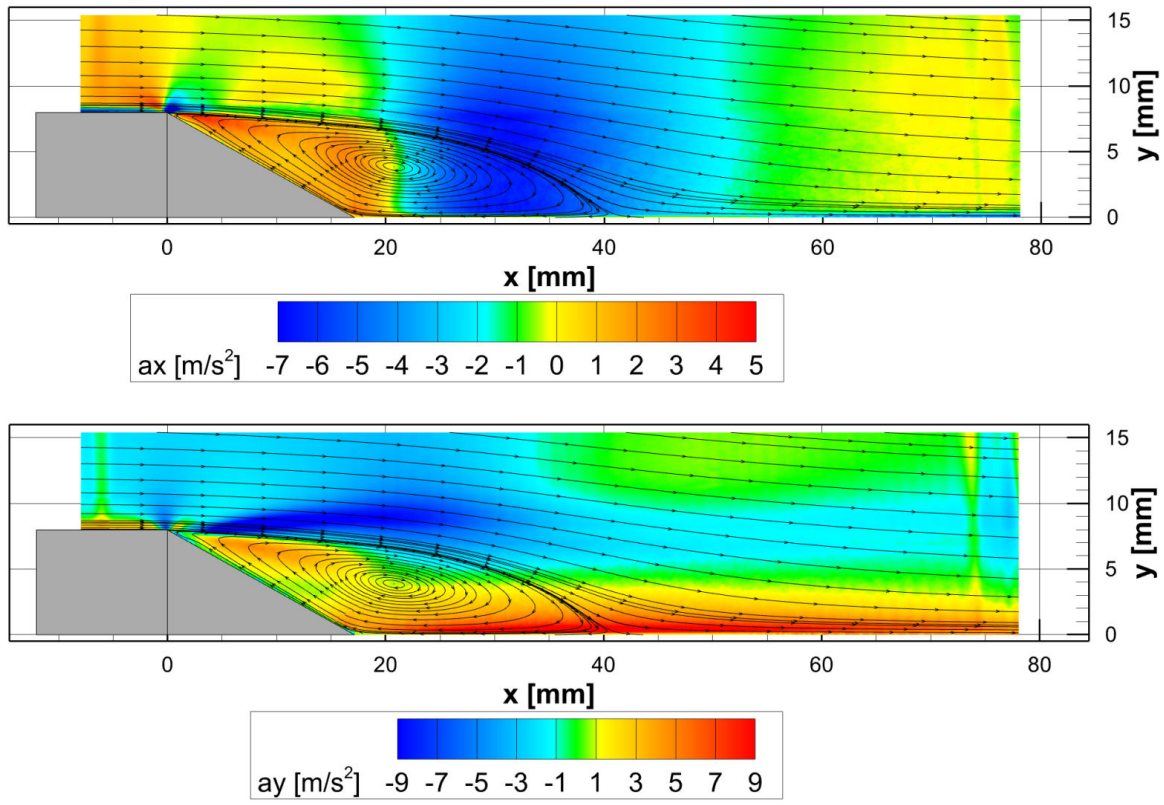

Figure 16: Time- and spanwise-averaged accelerations distributions. The flow exhibits positive and negative velocities, both in streamwise and wall normal direction. This implies that negative blue areas coupled with negative velocities are representing accelerations in the opposite direction

5. Conclusions

Separated turbulent flows are frequently observed in many research and industrial aerodynamic flow scenarios, such as flow over wings, spoilers, turbines, car bodies, and even buildings or bridges, and in general, these have a high-influence on overall aerodynamic behavior. A comprehensive characterization is required and could potentially lead to optimization in design, performance and safety. However, current statistical turbulence models, within the context of RANS equation, fail to predict the extent of

separation regions underneath turbulent or transitional shear flows. The presented work in the scope of the ADaMant project, has the primary aim to set a test case for improving and validating RANS turbulence models. Therefore, statistical converged profile results of the incoming TBL flow and of 2D bin-averaging results of the 3D particle tracks up- and downstream of the step and ramp down to the reorganization of TBL flow after reattachment has been delivered. A secondary aim is a knowledge improvement of scientific concerns, mainly related to the structure of turbulence in free shear layers. 3D Shake-The-Box was employed to capture the dynamics of a turbulent boundary layer developed over a flat plate at nearly-zero pressure gradient, followed by separation over a backward-facing ramp in the Große Wasserkanal Braunschweig (GWB) at $Re = 1.2 \times 10^6$, 1.6×10^6, 2.2×10^6, 2.7×10^6. Five high-speed cameras were placed on the side of the 6 x 1 x 1 m^3 test section, recording ORGASOL® 2002 D NAT 1 particles illuminated by two high-speed lasers. Chunk mode was used to ensure statistical convergence, with three runs recorded as time-resolved datasets Due to the large amount of data, results are provided only for $Re = 1.2 \times 10^6$. Data assimilation was performed to visualize instantaneous flow structures. Statistics were evaluated using a binning-average approach to gain mean velocities, Reynolds stresses and accelerations. Additionally, results are provided for third-order velocity moments.
The measurement suffered strong reflections very close to the walls, making the evaluation of the reattachment length quite difficult. The distributions of Reynolds stresses highlight the turbulence mixing that occurs in the free shear layer, with a dampening of fluctuations in the recirculation bubble center. The streamwise acceleration confirms the link between stresses variations and pressure-driven acceleration effects, and represent a novel feature of this dataset.

References

Driver, D. M. & Seegmiller, H. L., 1985. Features of a reattaching turbulent shear layer in divergent channel flow. *AIAA Journal,* February, Band 23, p. 163–171.

Eisfeld, B., 2022. The importance of turbulent equilibrium for Reynolds-stress modeling. *Physics of Fluids,* February, Band 34, p. 025123.

Godbersen, P., Gesemann, S., Schanz, D. & Schröder, A., 2024. FlowFit3: Efficient Data Assimilation Of LPT Measurements. *Proceedings of the International Symposium on the Application of Laser and Imaging Techniques to Fluid Mechanics,* July, Band 21, p. 1–14.

Godbersen, P., Schanz, D. & Schröder, A., 2024. Peak-CNN: improved particle image localization using single-stage CNNs. *Experiments in Fluids,* October, Volume 65, p. 153.

Grabe, C., 2022. DLR-Project ADaMant: Adaptive, Data-driven Physical Modeling towards Border of Envelope Applications. *Deutscher Luft- und Raumfahrtkongress, 27-29 Sept. 2022, Dresden, Germany.*

Greenblatt, D. et al., 2006. Experimental Investigation of Separation Control Part 1: Baseline and Steady Suction. *AIAA Journal,* December, Band 44, p. 2820–2830.

Liu, T. et al., 2005. *Pressure and temperature sensitive paints.* Berlin: Springer.

Miozzi, M. & Costantini, M., 2021. Temperature and skin-friction maps on a lifting hydrofoil in a propeller wake. *Measurement Science and Technology,* Band 32, p. 114007.

Schanz, D., Gesemann, S. & Schröder, A., 2016. Shake-The-Box: Lagrangian particle tracking at high particle image densities. *Experiments in Fluids,* April, Volume 57, p. 70.

Schanz, D., Novara, M. & Schröder, A., 2021. *Shake-The-Box particle tracking with variable time-steps in flows with high velocity range (VT-STB).* Chicago, USA (online), ILLINOIS Tech / Paul V. Galvin Library, p. 1–11.

Schanz, D. et al., 2024. *Scanning Lagrangian Particle Tracking To Measure 3D Large Scale Aerodynamics Of Quadcopter Flight.* Lisbon, Portugal: Proceedings of the International Symposium on the Application of Laser and Imaging Techniques to Fluid Mechanics,.

Schröder, A. & Schanz, D., 2023. 3D Lagrangian Particle Tracking in Fluid Mechanics. *Annual Review of Fluid Mechanics,* Band 55, pp. 511-540.

Schröder, A. et al., 2018. *Investigation of a high Reynolds number turbulent boundary layer flow with adverse pressure gradients using PIV and 2D- and 3D- Shake-The-Box.* Lisbon, Portugal, Proceedings of the International Symposium on the Application of Laser and Imaging Techniques to Fluid Mechanics.